Supplement of Atmos. Chem. Phys., 25, 6633–6662, 2025
https://doi.org/10.5194/acp-25-6633-2025-supplement

Atmospheric Chemistry and Physics
Open Access
EGU

Supplement of

Pollution affects Arabian and Saharan dust optical properties in the eastern Mediterranean

Marilena Teri et al.

Correspondence to: Bernadett Weinzierl (bernadett.weinzierl@univie.ac.at)

S1 Data analysis and quality control of the Aurora 4000 nephelometer

The particle scattering coefficients were measured at three wavelengths ($\lambda_B = 450\,\mathrm{nm}$, $\lambda_G = 525\,\mathrm{nm}$, $\lambda_R = 635\,\mathrm{nm}$) using an Aurora 4000 nephelometer placed in the Falcon aircraft cabin behind the aerosol inlet system (in-cabin). The Aurora 4000 nephelometer has the unique feature of measuring the particle scattering coefficients for various angular sectors (ranging from the shutter position α to $180°$), including the total particle scattering coefficient (measured when $\alpha = 0°$).

During the A-LIFE field experiment, the Aurora 4000 nephelometer was mounted behind an isokinetic aerosol inlet (Schöberl et al., 2024) and measured the particle scattering coefficients for four angular sectors, with $\alpha = 0°, 20°, 50°, 90°$. This configuration enabled a temporal resolution of $6 - 15\,\mathrm{s}$. A calibration with particle-free air and CO_2 was performed at the beginning of the A-LIFE field experiment and it was checked several times during and after it. The data obtained from the Aurora 4000 nephelometer was corrected using the average of all calibration checks, following the procedure recommended by Anderson and Ogren (1998). Additionally, multiple particle-free air measurements were conducted before and during the measurement flights to verify and correct for any potential background drift resulting from alteration in conditions during the measurements or of the carrier gas. The combined uncertainty due to instrumental noise, calibration and background drift uncertainties for 1-minute data is $\sim 3\%$. The Rayleigh scattering coefficients were subtracted to obtain the Aurora 4000 particle scattering coefficients ($\sigma_{\mathrm{sp},\lambda}^{\text{Aurora 4000, }\alpha}$). All the particle scattering coefficients were converted to standard temperature and pressure ($273.15\,\mathrm{K}$, $1013.25\,\mathrm{hPa}$).

The total particle scattering coefficients ($\sigma_{\mathrm{sp},\lambda}$) were obtained by correcting $\sigma_{\mathrm{sp},\lambda}^{\text{Aurora 4000, }0°}$ for angular truncation and illumination as indicated in Teri et al. (2022), i.e., using the Anderson and Ogren (1998) method deploying the Scattering Ångström exponent (C_{SAE}) for cases with SAE < 2, and the Müller et al. (2012) correction C_{polar} for cases with SAE > 2. The assumed uncertainties for the angular correction are 13% and 2%, respectively. A median average was performed along selected flight sequences. For flight sequences data used in this work, the uncertainties of $\sigma_{\mathrm{sp},\lambda}$ including instrumental noise, calibration and background drift uncertainties, uncertainties of the correction to standard temperature and pressure, and the truncation error uncertainty, are within $13 - 30\%$.

S2 Data analysis and quality control of the Tricolor Absorption Photometer (TAP)

The particle absorption coefficient was measured using a Tricolor Absorption Photometer (TAP, Brechtel) installed in the Falcon aircraft cabin behind an isokinetic aerosol inlet (Schöberl et al., 2024) inside the aircraft cabin. Measurements were taken at three different wavelengths ($\lambda_B = 465\,\mathrm{nm}$, $\lambda_G = 520\,\mathrm{nm}$, $\lambda_R = 640\,\mathrm{nm}$). The well characterized and widely used glass fiber Pallflex E70-2075W filters with a diameter of $47\,\mathrm{mm}$ were used (e.g., Virkkula, 2010; Davies et al., 2019). The filter was changed before each flight and the white filter check was performed according to the manufacturer indication. The light transmission through the filter decreases with the sampling time from about 1 to 0.85. Any deviation from a steady decrease in the filter transmission can be attributed to variation in inlet pressure, which modifies the filter optical properties during ascent and descent of the aircraft, as noted by Petzold et al. (2011). To avoid such artifact, we analyzed the TAP data exclusively for sequences at a constant altitude.

The spot area was determined to be $43.9 \pm 2.3\,\mathrm{mm}^2$ by measuring the diameter of each of the 10 spots with a caliber. The TAP sample flow was controlled by a mass flow meter (MFM, Alicat scientific) downstream of the measurement cell and measured by an internal flow meter. The sample flow was calibrated with a bubble flow meter (Gilibrator 2, Gilian) by varying the pressure in the range $200 - 1000\,\mathrm{hPa}$. The obtained linear least-squares regression parameters (Slope$= 0.92$, Offset$= -0.03$, $R^2 > 0.999$) were used to correct the measured sample flow. The calculated actual volume flow rate was $1.6 \pm 0.2\,\mathrm{L/min}$. Data were converted to standard temperature and pressure ($273.15\,\mathrm{K}$; $1013.25\,\mathrm{hPa}$). Data sequences with the particle absorption coefficient below $0.6\,\mathrm{Mm}^{-1}$ at least at one wavelength at ambient conditions were considered below the detection limit and excluded from the analysis. This decision follows the guidelines of the TAP user manual and Ogren et al. (2017).

The particle absorption coefficient was corrected for filter loading and scattering effects with the correction scheme developed by Virkkula et al. (2005) and modified by Virkkula (2010), using the particle scattering coefficient corrected for angular truncation and illumination error. This correction scheme was developed for the Particle Soot Absorption Photometer (PSAP, Radiance Reasearch) and its performance was tested for the TAP by Davies et al. (2019). Their study calculated biases in the

particle absorption coefficient measured by the TAP for urban aerosol of 38 %, 37 %, and 27 % for the blue, green, and red wavelengths, respectively. We assumed an uncertainty of 40 % for all three wavelengths, considering that the wavelengths of our TAP are slightly different from the TAP used by Davies et al. (2019).

We conducted additional data quality checks by comparing the particle absorption coefficient with the mass of refractory black carbon (M_{rBC}) measured by a Single Particle Soot Photometer (SP2). A correlation is expected between these two quantities since black carbon is the most important aerosol absorption component (e.g., Bond et al., 2013). We found a strong correlation with $R^2 > 0.92$ at all three wavelengths when excluding data points collected at pressure conditions lower than 400 hPa (see Figure S1). Data points collected at lower pressure appeared noisier and were excluded from our data. The high correlation between the particle absorption coefficient and the mass of refractory black carbon provided further evidence of the quality of the TAP data.

Additionally, we calculated the mass absorption coefficients ($\mathrm{MAC_{corr}}$) from the correlation of the two quantities. We obtained values of $19.4\ \mathrm{m^2 g^{-1}}$, $15.9\ \mathrm{m^2 g^{-1}}$, and $10\ \mathrm{m^2 g^{-1}}$ for the wavelengths blue, green, and red respectively. These values are of the order of magnitude expected in literature for black carbon. For example, Ohata et al. (2021) reported values in the range of $10.8 - 15.1\ \mathrm{m^2 g^{-1}}$ for the $\mathrm{MAC_{corr}}$ measured in the Arctic at the green wavelength ($\lambda = 550$ nm). Our values are slightly higher because the particle absorption coefficient measured by the TAP instrument includes the contribution of mineral dust, which is also expected to absorb in the blue and green wavelengths.

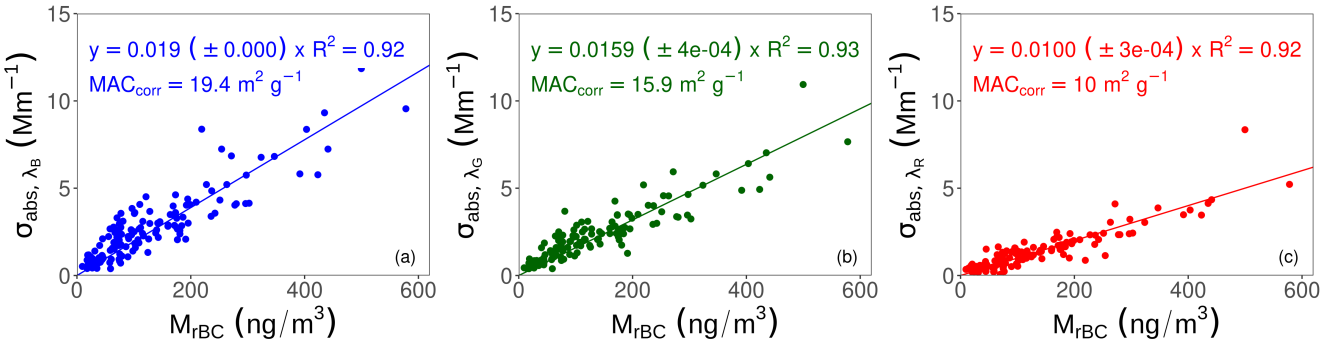

Figure S1. TAP data quality. The three panels (a, b, and c) show the comparison between the particle absorption coefficients ($\sigma_{\mathrm{abs},\lambda}$) at $\lambda = 465$, 520, and 640 nm, respectively, and the mass concentration of refractory black carbon (M_{rBC}). Results from linear regression analysis and corresponding mass absorption coefficient (MAC) values are reported on each figure.

S3 Extension of g_λ and SSA_λ to the ambient number size distribution

The asymmetry parameter (g) and the single-scattering albedo (SSA) were calculated from the particle scattering and absorption coefficients measured in the aircraft cabin behind an aerosol sampling system (see section 2.3.2 of the main text). Thus, the obtained g and SSA values are representative of the measured aerosol particles in the size range passing through the Falcon aerosol inlet and transport system, and thus, for the in-cabin number size distributions (NSDs). We calculated the values of g and SSA representative of the ambient NSDs ($g_{\lambda,\text{ambient}}$ and $\mathrm{SSA}_{\lambda,\text{ambient}}$) by multiplying the measured g and SSA values ($g_{\lambda,\text{in-cabin}}$ and $\mathrm{SSA}_{\lambda,\text{in-cabin}}$) with a factor.

To calculate the correction factor to extend the measured optical properties to the ambient NSD, we performed optical simulations using the in-cabin and ambient NSDs as input of the MOPSMAP program (Gasteiger and Wiegner, 2018). The ambient NSDs were used in ambient relative humidity, while the in-cabin NDSs were used in dry conditions. The simulated optical properties were derived at three wavelengths ($\lambda_B = 450\,\mathrm{nm}$, $\lambda_G = 525\,\mathrm{nm}$, $\lambda_B = 635\,\mathrm{nm}$) considering the modeled aerosol composition (see section 2.3.5 in the main text). While mineral dust particles were assumed to be spheroids with an aspect ratio distribution according to Kandler et al. (2009), the other particle types were assumed to be spherical. The dust refractive index was taken from OPAC (Hess et al., 1998) in combination with a non-absorbing fraction of 0.5 (Gasteiger and Wiegner, 2018). Refractive indices from Li (1976) for sea salt, from Moise et al. (2015) for organic matter, and from Hess et al. (1998) for soot were considered, while a value of $1.53 + 0.00i$ was assumed for sulfate (e.g., Toon et al., 1976).

Figure S2 shows the comparison between the simulated and directly measured in-cabin intensive optical properties $g_{\lambda,\text{in-cabin}}$ and $SSA_{\lambda,\text{in-cabin}}$ at wavelengths 450, 525, and $635\,\mathrm{nm}$. The directly measured intensive optical properties are reproduced by this approach within $\sim 16\%$ for $g_{\lambda,\text{in-cabin}}$ and within $\sim 10\%$ for $SSA_{\lambda,\text{in-cabin}}$. This comparison provides evidence that the approach used to extend the in situ measured optical properties to ambient conditions is sufficiently accurate. A deeper discussion of the discrepancies between model simulations and measured optical properties is out of the scope of this paper.

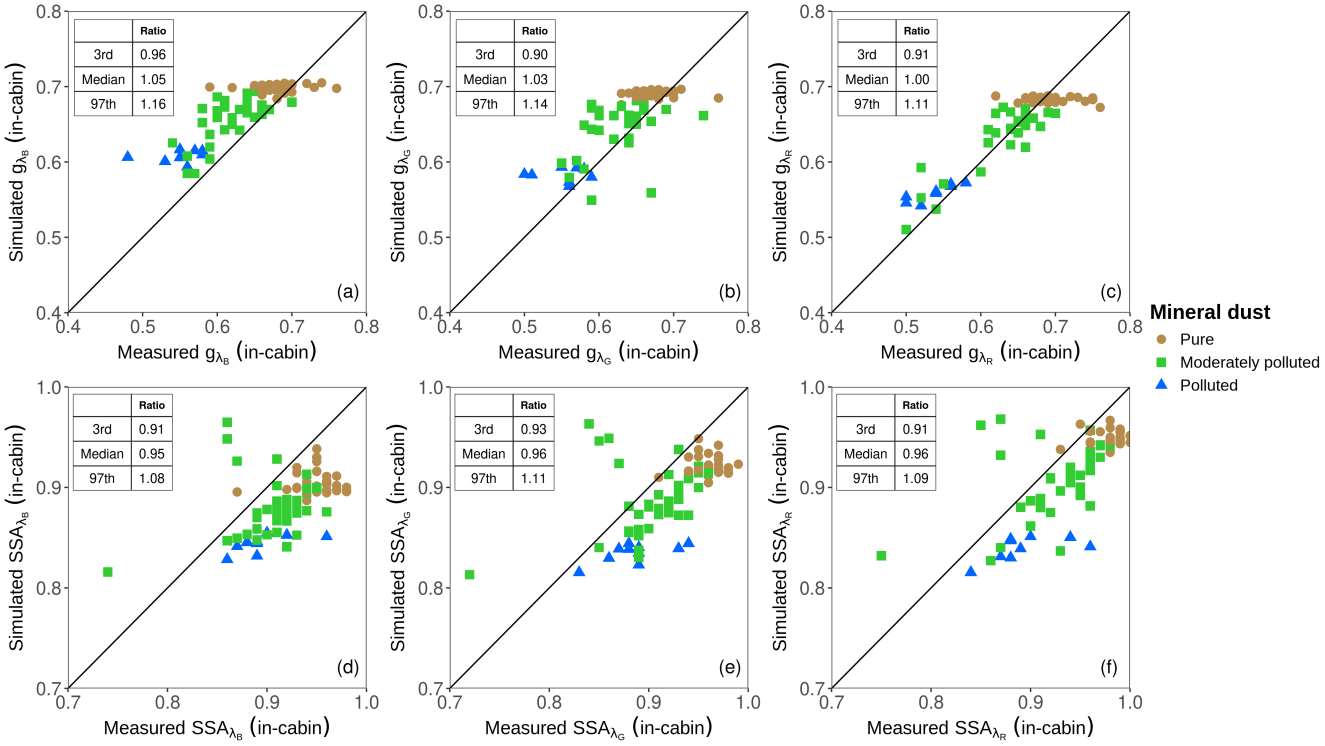

Figure S2. Comparison between the simulated intensive optical properties representative for the in-cabin NSD, and the intensive aerosol optical properties measured in the cabin of the Falcon research aircraft behind an inlet and a sampling system (in-cabin). Panels (a,b, and c) show the comparison for the simulated $g_{\lambda,\text{in-cabin}}$ and the measured $g_{\lambda,\text{in-cabin}}$ at wavelengths 450, 525, and 635 nm, respectively. Panels (d, e, and f) show the comparison for simulated $SSA_{\lambda,\text{in-cabin}}$ and the simulated $SSA_{\lambda,\text{in-cabin}}$ at wavelengths 450, 525, and 635 nm, respectively. The colors and shapes indicate the aerosol types following the A-LIFE aerosol classification scheme. The one to one line is shown in black. The median, 3rd, and 97th percentiles of the ratios between the simulated and measured values are reported in the upper left corner of the plots.

The correction factor to extend the intensive optical properties to the ambient NSD $(0.01 - 50\,\mu\text{m})$ was calculated as the ratio of the simulated property for the ambient NSD and the simulated property for the in-cabin NSD:

$$g_{\lambda,\text{ambient}} = g_{\lambda,\text{in-cabin}} \cdot \frac{\text{simulated } g_{\lambda,\text{ambient}}}{\text{simulated } g_{\lambda,\text{in-cabin}}} \tag{S1}$$

$$SSA_{\lambda,\text{ambient}} = SSA_{\lambda,\text{in-cabin}} \cdot \frac{\text{simulated } SSA_{\lambda,\text{ambient}}}{\text{simulated } SSA_{\lambda,\text{in-cabin}}} \tag{S2}$$

Figure S3 shows the comparisons between the simulated optical properties representative of the ambient NSDs and the simulated optical properties representative of the in-cabin NSDs. For each sequence, the deviation from the one-to-one line represents the correction factor applied to extend the intensive optical properties to the ambient NSD.

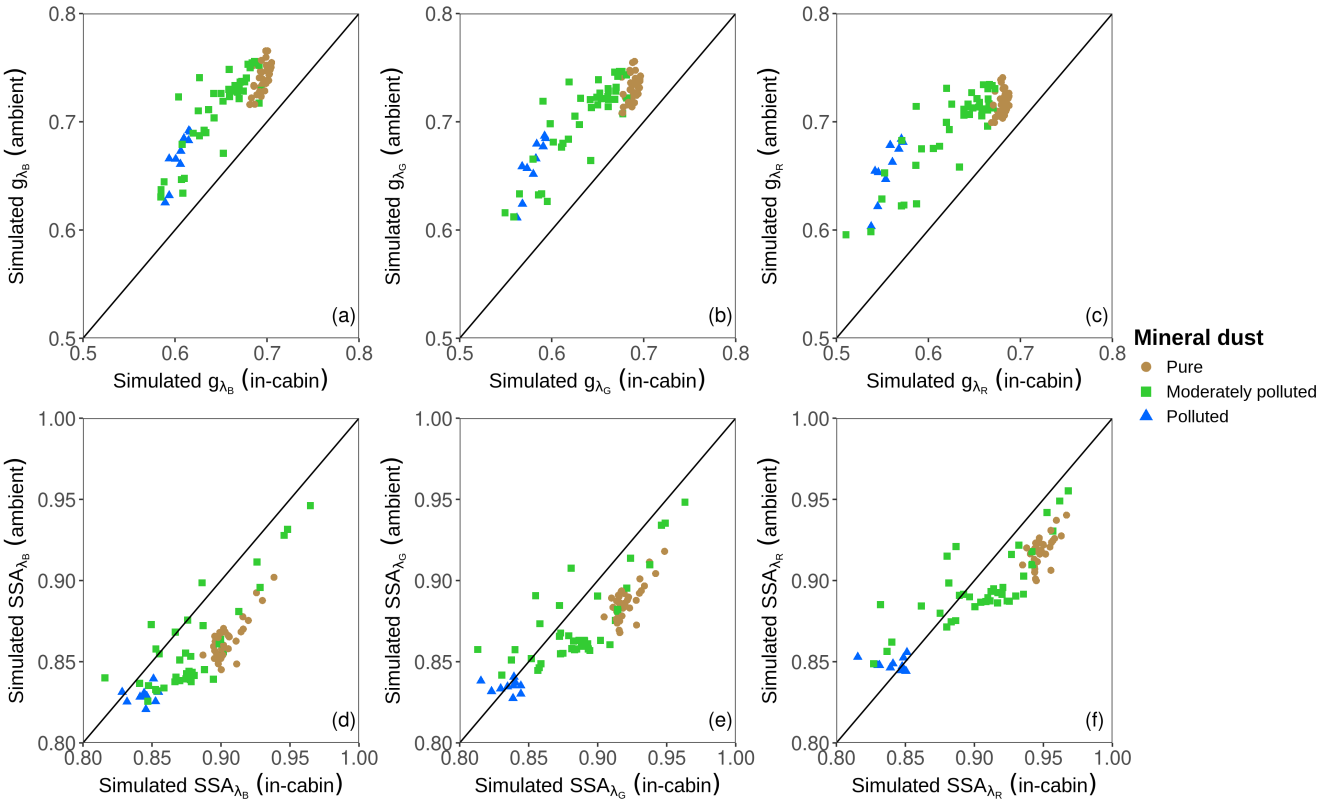

Figure S3. Simulated aerosol optical properties representative of the ambient NSD in comparison with the simulated aerosols optical properties representative of the in-cabin NSD. Panels (a,b, and c) show the comparison for the simulated $g_{\lambda,\text{ambient}}$ and the simulated $g_{\lambda,\text{in-cabin}}$ at wavelengths 450, 525, and 635 nm, respectively. Panels (d, e, and f) show the comparison for simulated $SSA_{\lambda,\text{ambient}}$ and the simulated $SSA_{\lambda,\text{in-cabin}}$ at wavelengths 450, 525, and 635 nm, respectively. The colors and shapes indicate the aerosol types following the A-LIFE aerosol classification scheme. The one to one line is shown in black.

S4 Single-particle chemistry analysis of mineral dust particles collected during the A-LIFE field experiment

To support the interpretation of our results, we also used data from the single-particle chemistry analysis of in situ samples collected during the A-LIFE field experiment. A micro inertial impactor (MINI) sampler collecting particles with diameters smaller than $1\ \mu m$ and larger than $1\ \mu m$ (Kandler et al., 2007) was placed in the Falcon aircraft cabin behind the aerosol inlet system (Schöberl et al., 2024). Particles were collected on transmission electron microscope (TEM) grids and boron substrates, with sampling time varying from three to ten minutes for each sample. Subsequently, the characteristics of single particles were studied under high vacuum conditions by an automated analysis in a environmental scanning electron microscope (FEI ESEM Quanta 400 FEG instrument, Eindhoven, The Netherlands) coupled with an X-Max 150 energy-dispersive X-ray spectroscopy (EDX) silicon drift X-ray detector (Oxford). Thus, the morphology and elemental composition of each particle (with projected area diameter from 0.5 to $3.0\ \mu m$) consisting of major elements F, Na, Mg, Al, Si, P, S, Cl, K, Ca, Ti, V, Cr, Mn, Fe, Zn and Pb is derived from EDX and given as normalized atomic percentages. The major dust components which are commonly found as 'internal mixtures' or aggregates were classified into dust particle-types by keeping each particles Al/Si ratios as the main constraint (Kandler et al., 2007). More details on the classification of the particle types used in this work are published and can be found as supplement data in (Panta et al., 2023).

The mineral dust optical properties for each sample are calculated using an empirical approach derived from Di Biagio et al. (2019) and used by Kandler et al. (2020) and detailed in Aryasree et al. (2024) for particles from various mineral dust sources. The empirical relation links the total iron (Fe) present in mineral dust particles as oxides with the optical properties of mineral dust particles, such as the imaginary part of the refractive index (k) and the single-scattering albedo (SSA).

S4.1 Mineral dust composition from single-particle analysis

Data from the single-particle chemistry analysis are used to support the interpretation of results of this work. Figure S4 shows the percentage abundances of seven particle-type classes for Arabian and Saharan dust samples. The 7 particle-type classes were obtained from about 8000 particles measured under the scanning electron microscope. The analyzed samples were collected during flight sequences classified as pure and moderately polluted Arabian and Saharan dust according to the A-LIFE aerosol classification (see section 2.3.4 in the main text). Additionally, Figure S5 shows different element ratios for particles in Arabian and Saharan dust sequences. Arabian and Saharan dust samples show a similar abundance with a higher percentage of Si-rich particles or low Al/Si ratio particles named silicate-like particles hereafter. Mineral dust particles from both source regions have $60-62\%$ of these silicate-like particles. Additionally, we observed a negligible variance in the illite to kaolinite (I/K) ratio, which is often used, in combination with ratios of other clay minerals-like particles, as a fingerprint to the active source regions Scheuvens et al. (2013). The most significant difference observed in the mineralogy composition is a higher abundance of clay-like minerals (illite and kaolinite) from the Sahara (21% against 8% for Arabian dust). While carbonate (e.g., calcite, dolomite etc.) content is higher in Arabian dust (18%), a lower percentage is measured in Saharan dust (6%). This result is in agreement with several previous studies conducted in Saharan near-source regions, as well as in regions where mineral dust is transported, which characterize Saharan dust particles as having a higher clay mineral content (Kandler et al., 2009; Formenti et al., 2011). However, there are only limited studies in the Middle East and nearby Arabian dust sources to characterize the mineralogical characteristics of the Arabian dust (Attiya and Jones, 2020; Engelbrecht et al., 2009, 2016). All these studies show high variability in mineral dust and soil mineralogy within the Arabian Peninsula, making it difficult to find an exact dust mineralogical characteristic. However, compared to Saharan dust, a high carbonate and low clay content is common in these studies. The percentage of iron oxides and hydroxides in Arabian dust is half that of the Saharan (3%, see Figure S4). To obtain a more accurate iron content description, we calculated iron's total oxide percentage for each mineral dust particle using Table 3 values from Di Biagio et al. (2019) and the Fe mass of the particle. A summary of this method is available in Kandler et al. (2020). For statistical certainty bootstrapping was done with 10,000 particles for the dust sequences. The result shows a $\sim 10\%$ increase in the total iron oxide weight in Saharan dust (median: 8.65 at a 95% confidence interval of $8.2-8.9$) as compared to the Arabian dust median value of 7.8 (95% confidence interval of $7.6-8.1$).

Since the mineral dust optical properties depend on the total iron content, this result indicates that the Saharan dust particles were more absorbing than the Arabian dust particles over the eastern Mediterranean. Indeed, the imaginary part of the refractive index (k) has a value of 0.006 for Saharan dust and 0.005 for Arabian dust (see Figure S6). The SSA of mineral dust particles

showed a 4% increase for Arabian dust compared to Saharan dust. The imaginary refractive index values of mineral dust particles are higher than the characteristics of Saharan dust as seen from other locations over Northwest Sahara or the mineral dust outflow regions in the Atlantic (e.g., $0.001 - 0.004$ at $520\ \mathrm{nm}$ Cape Verde) (Kandler et al., 2007, 2011; Haywood et al., 2008).

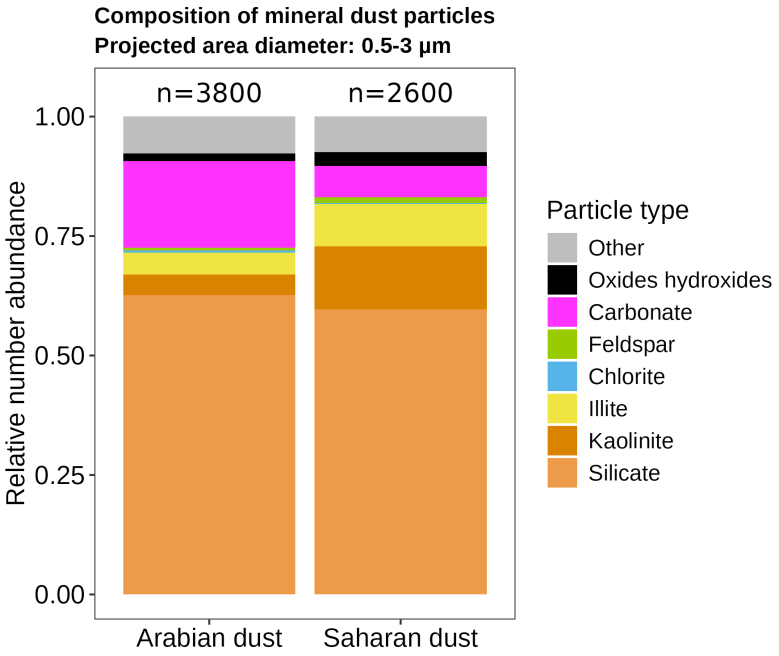

Figure S4. Composition of mineral dust particles with projected area diameter ranging from 0.5 to 3 µm. The graphs show the relative abundance of 7 dust particle types, as observed under the scanning electron microscope, for samples collected during sequences classified as Arabian and Saharan dust according to the A-LIFE aerosol classification scheme. The pollution degree is not considered as only mineral dust particles are observable in this size range. The number of particles (n) analyzed is above the corresponding bar.

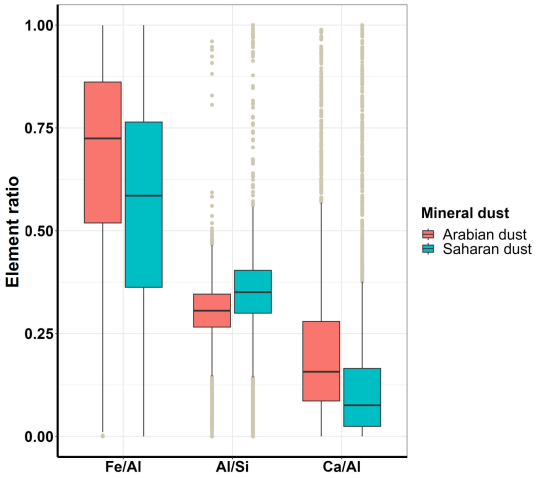

Figure S5. Element ratios (Fe/Al, Al/Si, Ca/Al) for Saharan and Arabian dust particles. The graph shows three elemental ratios obtained from about 8000 particles measured under the scanning electron microscope. The analyzed samples were collected during flight sequences classified as pure and moderately polluted Arabian dust and Saharan dust according to the A-LIFE aerosol classification scheme. The boxes represent the interquartile range (IQR $25th - 75th$), the horizontal lines the median, the whiskers the largest value that is not greater than $1.5 \cdot IQR$, and data points outside this range are shown as individual dots.

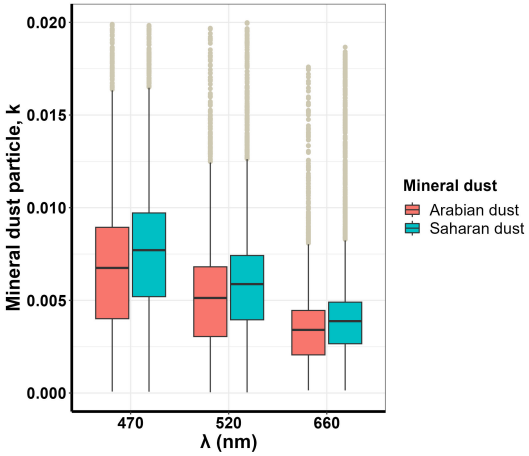

Figure S6. Spectral imaginary dust refractive index for Arabian and Saharan dust. The graph shows the median values of the imaginary part of the refractive index at three wavelengths obtained from single-particle chemistry analysis. The analyzed samples were collected during flight sequences classified as pure and moderately polluted Arabian dust and Saharan dust according to the A-LIFE aerosol classification scheme. The boxes represent the interquartile range (IQR $25th - 75th$), the horizontal lines the median, the whiskers the largest value that is not greater than $1.5 \cdot IQR$, and data points outside this range are shown as individual dots.

References

Anderson, T. L. and Ogren, J. A.: Determining Aerosol Radiative Properties Using the TSI 3563 Integrating Nephelometer, Aerosol Science and Technology, 29, 57–69, https://doi.org/10.1080/02786829808965551, 1998.

Aryasree, S., Kandler, K., Benker, N., Walser, A., Tipka, A., Dollner, M., Seibert, P., and Weinzierl, B.: Vertical Variability in Morphology, Chemistry and Optical Properties of the Transported Saharan Air Layer Measured from Cape Verde and the Caribbean, Royal Society Open Science, 11, 231 433, https://doi.org/10.1098/rsos.231433, 2024.

Attiya, Ali. A. and Jones, B. G.: Assessment of Mineralogical and Chemical Properties of Airborne Dust in Iraq, SN Applied Sciences, 2, 1614, https://doi.org/10.1007/s42452-020-03326-5, 2020.

Bond, T. C., Doherty, S. J., Fahey, D. W., Forster, P. M., Berntsen, T., DeAngelo, B. J., Flanner, M. G., Ghan, S., Kärcher, B., Koch, D., Kinne, S., Kondo, Y., Quinn, P. K., Sarofim, M. C., Schultz, M. G., Schulz, M., Venkataraman, C., Zhang, H., Zhang, S., Bellouin, N., Guttikunda, S. K., Hopke, P. K., Jacobson, M. Z., Kaiser, J. W., Klimont, Z., Lohmann, U., Schwarz, J. P., Shindell, D., Storelvmo, T., Warren, S. G., and Zender, C. S.: Bounding the Role of Black Carbon in the Climate System: A Scientific Assessment, Journal of Geophysical Research: Atmospheres, 118, 5380–5552, https://doi.org/10.1002/jgrd.50171, 2013.

Davies, N. W., Fox, C., Szpek, K., Cotterell, M. I., Taylor, J. W., Allan, J. D., Williams, P. I., Trembath, J., Haywood, J. M., and Langridge, J. M.: Evaluating Biases in Filter-Based Aerosol Absorption Measurements Using Photoacoustic Spectroscopy, Atmospheric Measurement Techniques, 12, 3417–3434, https://doi.org/10.5194/amt-12-3417-2019, 2019.

Di Biagio, C., Formenti, P., Balkanski, Y., Caponi, L., Cazaunau, M., Pangui, E., Journet, E., Nowak, S., Andreae, M. O., Kandler, K., Saeed, T., Piketh, S., Seibert, D., Williams, E., and Doussin, J.-F.: Complex Refractive Indices and Single-Scattering Albedo of Global Dust Aerosols in the Shortwave Spectrum and Relationship to Size and Iron Content, Atmospheric Chemistry and Physics, 19, 15 503–15 531, https://doi.org/10.5194/acp-19-15503-2019, 2019.

Engelbrecht, J. P., McDonald, E. V., Gillies, J. A., "Jay" Jayanty, R. K., Casuccio, G., and Gertler, A. W.: Characterizing Mineral Dusts and Other Aerosols from the Middle East—Part 2: Grab Samples and Re-Suspensions, Inhalation Toxicology, 21, 327–336, https://doi.org/10.1080/08958370802464299, 2009.

Engelbrecht, J. P., Moosmüller, H., Pincock, S., Jayanty, R. K. M., Lersch, T., and Casuccio, G.: Technical Note: Mineralogical, Chemical, Morphological, and Optical Interrelationships of Mineral Dust Re-Suspensions, Atmospheric Chemistry and Physics, 16, 10 809–10 830, https://doi.org/10.5194/acp-16-10809-2016, 2016.

Formenti, P., Schütz, L., Balkanski, Y., Desboeufs, K., Ebert, M., Kandler, K., Petzold, A., Scheuvens, D., Weinbruch, S., and Zhang, D.: Recent Progress in Understanding Physical and Chemical Properties of African and Asian Mineral Dust, Atmospheric Chemistry and Physics, 11, 8231–8256, https://doi.org/10.5194/acp-11-8231-2011, 2011.

Gasteiger, J. and Wiegner, M.: MOPSMAP v1.0: A Versatile Tool for the Modeling of Aerosol Optical Properties, Geoscientific Model Development, 11, 2739–2762, https://doi.org/10.5194/gmd-11-2739-2018, 2018.

Haywood, J. M., Pelon, J., Formenti, P., Bharmal, N., Brooks, M., Capes, G., Chazette, P., Chou, C., Christopher, S., Coe, H., Cuesta, J., Derimian, Y., Desboeufs, K., Greed, G., Harrison, M., Heese, B., Highwood, E. J., Johnson, B., Mallet, M., Marticorena, B., Marsham, J., Milton, S., Myhre, G., Osborne, S. R., Parker, D. J., Rajot, J.-L., Schulz, M., Slingo, A., Tanré, D., and Tulet, P.: Overview of the Dust and Biomass-burning Experiment and African Monsoon Multidisciplinary Analysis Special Observing Period-0, Journal of Geophysical Research: Atmospheres, 113, https://doi.org/10.1029/2008JD010077, 2008.

Hess, M., Koepke, P., and Schult, I.: Optical Properties of Aerosols and Clouds: The Software Package OPAC, Bulletin of the American Meteorological Society, 79, 831–844, https://doi.org/10.1175/1520-0477(1998)079<0831:OPOAAC>2.0.CO;2, 1998.

Kandler, K., Benker, N., Bundke, U., Cuevas, E., Ebert, M., Knippertz, P., Rodríguez, S., Schütz, L., and Weinbruch, S.: Chemical Composition and Complex Refractive Index of Saharan Mineral Dust at Izaña, Tenerife (Spain) Derived by Electron Microscopy, Atmospheric Environment, 41, 8058–8074, https://doi.org/10.1016/j.atmosenv.2007.06.047, 2007.

Kandler, K., SchüTZ, L., Deutscher, C., Ebert, M., Hofmann, H., JäCKEL, S., Jaenicke, R., Knippertz, P., Lieke, K., Massling, A., Petzold, A., Schladitz, A., Weinzierl, B., Wiedensohler, A., Zorn, S., and Weinbruch1, S.: Size Distribution, Mass Concentration, Chemical and Mineralogical Composition and Derived Optical Parameters of the Boundary Layer Aerosol at Tinfou, Morocco, during SAMUM 2006, Tellus B: Chemical and Physical Meteorology, 61, 32–50, https://doi.org/10.1111/j.1600-0889.2008.00385.x, 2009.

Kandler, K., Lieke, K., Benker, N., Emmel, C., Küpper, M., Müller-Ebert, D., Ebert, M., Scheuvens, D., Schladitz, A., Schütz, L., and Weinbruch, S.: Electron Microscopy of Particles Collected at Praia, Cape Verde, during the Saharan Mineral Dust Experiment: Particle Chemistry, Shape, Mixing State and Complex Refractive Index, Tellus B: Chemical and Physical Meteorology, 63, 475–496, https://doi.org/10.1111/j.1600-0889.2011.00550.x, 2011.

Kandler, K., Schneiders, K., Heuser, J., Waza, A., Aryasree, S., Althausen, D., Hofer, J., Abdullaev, S. F., and Makhmudov, A. N.: Differences and Similarities of Central Asian, African, and Arctic Dust Composition from a Single Particle Perspective, Atmosphere, 11, 269, https://doi.org/10.3390/atmos11030269, 2020.

Li, H. H.: Refractive Index of Alkali Halides and Its Wavelength and Temperature Derivatives, Journal of Physical and Chemical Reference Data, 5, 329–528, https://doi.org/10.1063/1.555536, 1976.

Moise, T., Flores, J. M., and Rudich, Y.: Optical Properties of Secondary Organic Aerosols and Their Changes by Chemical Processes, Chemical Reviews, 115, 4400–4439, https://doi.org/10.1021/cr5005259, 2015.

Müller, T., Paixão, M., Pfeifer, S., and Wiedensohler, A.: Scattering Coefficients and Asymmetry Parameters Derived from the ! Polar Nephelometer Aurora4000!, p. 1, 2012.

Ogren, J. A., Wendell, J., Andrews, E., and Sheridan, P. J.: Continuous Light Absorption Photometer for Long-Term Studies, Atmospheric Measurement Techniques, 10, 4805–4818, https://doi.org/10.5194/amt-10-4805-2017, 2017.

Ohata, S., Mori, T., Kondo, Y., Sharma, S., Hyvärinen, A., Andrews, E., Tunved, P., Asmi, E., Backman, J., Servomaa, H., Veber, D., Eleftheriadis, K., Vratolis, S., Krejci, R., Zieger, P., Koike, M., Kanaya, Y., Yoshida, A., Moteki, N., Zhao, Y., Tobo, Y., Matsushita, J., and Oshima, N.: Estimates of Mass Absorption Cross Sections of Black Carbon for Filter-Based Absorption Photometers in the Arctic, Atmospheric Measurement Techniques, 14, 6723–6748, https://doi.org/10.5194/amt-14-6723-2021, 2021.

Panta, A., Kandler, K., Alastuey, A., González-Flórez, C., González-Romero, A., Klose, M., Querol, X., Reche, C., Yus-Díez, J., and Pérez García-Pando, C.: Insights into the Single-Particle Composition, Size, Mixing State, and Aspect Ratio of Freshly Emitted Mineral Dust from Field Measurements in the Moroccan Sahara Using Electron Microscopy, Atmospheric Chemistry and Physics, 23, 3861–3885, https://doi.org/10.5194/acp-23-3861-2023, 2023.

Petzold, A., Veira, A., Mund, S., Esselborn, M., Kiemle, C., Weinzierl, B., Hamburger, T., Ehret, G., Lieke, K., and Kandler, K.: Mixing of Mineral Dust with Urban Pollution Aerosol over Dakar (Senegal): Impact on Dust Physico-Chemical and Radiative Properties, Tellus B: Chemical and Physical Meteorology, 63, 619–634, https://doi.org/10.1111/j.1600-0889.2011.00547.x, 2011.

Scheuvens, D., Schütz, L., Kandler, K., Ebert, M., and Weinbruch, S.: Bulk Composition of Northern African Dust and Its Source Sediments — A Compilation, Earth-Science Reviews, 116, 170–194, https://doi.org/10.1016/j.earscirev.2012.08.005, 2013.

Schöberl, M., Dollner, M., Gasteiger, J., Seibert, P., Tipka, A., and Weinzierl, B.: Characterization of the Airborne Aerosol Inlet and Transport System Used during the A-LIFE Aircraft Field Experiment, Atmospheric Measurement Techniques, 17, 2761–2776, https://doi.org/10.5194/amt-17-2761-2024, 2024.

Teri, M., Müller, T., Gasteiger, J., Valentini, S., Horvath, H., Vecchi, R., Bauer, P., Walser, A., and Weinzierl, B.: Impact of Particle Size, Refractive Index, and Shape on the Determination of the Particle Scattering Coefficient – an Optical Closure Study Evaluating Different Nephelometer Angular Truncation and Illumination Corrections, Atmospheric Measurement Techniques, 15, 3161–3187, https://doi.org/10.5194/amt-15-3161-2022, 2022.

Toon, O. B., Pollack, J. B., and Khare, B. N.: The Optical Constants of Several Atmospheric Aerosol Species: Ammonium Sulfate, Aluminum Oxide, and Sodium Chloride, Journal of Geophysical Research (1896-1977), 81, 5733–5748, https://doi.org/10.1029/JC081i033p05733, 1976.

Virkkula, A.: Correction of the Calibration of the 3-Wavelength Particle Soot Absorption Photometer (3λ PSAP), Aerosol Science and Technology, 44, 706–712, https://doi.org/10.1080/02786826.2010.482110, 2010.

Virkkula, A., Ahlquist, N. C., Covert, D. S., Arnott, W. P., Sheridan, P. J., Quinn, P. K., and Coffman, D. J.: Modification, Calibration and a Field Test of an Instrument for Measuring Light Absorption by Particles, Aerosol Science and Technology, 39, 68–83, https://doi.org/027868290901963, 2005.